



## The significance of the spectral correction of photon counting detector response in material classification from spectral x-ray CT

Jumanazarov, Doniyor; Koo, Jakeoung; Poulsen, Henning F.; Olsen, Ulrik L.; lovea, Mihai

*Published in:*  
Quantum Optics and Photon Counting 2021

*Link to article, DOI:*  
[10.1117/12.2589290](https://doi.org/10.1117/12.2589290)

*Publication date:*  
2021

*Document Version*  
Publisher's PDF, also known as Version of record

[Link back to DTU Orbit](#)

*Citation (APA):*  
Jumanazarov, D., Koo, J., Poulsen, H. F., Olsen, U. L., & lovea, M. (2021). The significance of the spectral correction of photon counting detector response in material classification from spectral x-ray CT. In *Quantum Optics and Photon Counting 2021* (Vol. 11771). Article 117710J SPIE - International Society for Optical Engineering. <https://doi.org/10.1117/12.2589290>

---

### General rights

Copyright and moral rights for the publications made accessible in the public portal are retained by the authors and/or other copyright owners and it is a condition of accessing publications that users recognise and abide by the legal requirements associated with these rights.

- Users may download and print one copy of any publication from the public portal for the purpose of private study or research.
- You may not further distribute the material or use it for any profit-making activity or commercial gain
- You may freely distribute the URL identifying the publication in the public portal

If you believe that this document breaches copyright please contact us providing details, and we will remove access to the work immediately and investigate your claim.

# PROCEEDINGS OF SPIE

[SPIDigitalLibrary.org/conference-proceedings-of-spie](https://spiedigitallibrary.org/conference-proceedings-of-spie)

## The significance of the spectral correction of photon counting detector response in material classification from spectral x-ray CT

Jumanazarov, Doniyor, Koo, Ja-Keoung, Poulsen, Henning, Olsen, Ulrik, Iovea, Mihai

Doniyor Jumanazarov, Ja-Keoung Koo, Henning F. Poulsen, Ulrik L. Olsen, Mihai Iovea, "The significance of the spectral correction of photon counting detector response in material classification from spectral x-ray CT," Proc. SPIE 11771, Quantum Optics and Photon Counting 2021, 117710J (18 April 2021); doi: 10.1117/12.2589290

**SPIE.**

Event: SPIE Optics + Optoelectronics, 2021, Online Only

# The significance of the spectral correction of photon counting detector response in material classification from spectral X-ray CT

Doniyor Jumanazarov<sup>a,c</sup>, Jakeoung Koo<sup>b</sup>, Henning F. Poulsen<sup>a</sup>, Ulrik L. Olsen<sup>a</sup>, and Mihai IOVEA<sup>c</sup>

<sup>a</sup>Technical University of Denmark, DTU Physics, 2800 Kgs. Lyngby, Denmark

<sup>b</sup>Technical University of Denmark, DTU Compute, 2800 Kgs. Lyngby, Denmark

<sup>c</sup>ACCENT PRO 2000 s.r.l. (AP2K), Nerva Traian 1, K6, Ap. 26, Bucharest, S3, ROMANIA  
031041

## ABSTRACT

Photon counting imaging detectors (PCD) has paved the way for the emergence of Spectral X-ray Computed Tomography (SCT), which simultaneously measures a material's linear attenuation coefficient (LAC) at multiple energies defined by the energy thresholds. In previous work SCT data was analysed with the SIMCAD method for material classifications. The method measures system-independent material properties such as electron density,  $\rho_e$  and effective atomic number,  $Z_{\text{eff}}$  to identify materials in security applications. The method employs a spectral correction algorithm that reduce the primary spectral distortions from the raw data that arise from the detector response: charge sharing and weighting potential cross-talk, fluorescence radiation, scattering radiation, pulse pile up and incomplete charge collection. In this work, using real experimental data we analyze the influence of the spectral correction on material classification performance in security applications. We use a vectorial total variation ( $L_\infty$ -VTV) as a convex regularizer for image reconstruction of the spectral sinogram. This reconstruction algorithm employs a  $L_\infty$  norm to penalize the violation of the inter energy bin dependency, resulting in strong coupling among energy bins. Due to the strong inter-bin correlation,  $L_\infty$ -VTV leads to noticeably better performance compared to bin-by-bin reconstructions including SIRT and total variation (TV) reconstruction algorithms. The image quality was evaluated with the correlation coefficient that is computed relative to ground-truth images. A positive weighting parameter defines the strength of the  $L_\infty$ -VTV regularization term and thus controls the trade-off between a good match to spectral sinogram data and a smooth reconstruction in both the spatial and spectral dimension. The classification accuracy both for raw and corrected data is analyzed over a set of weighting parameters. For material classification, we used 20 different materials for calibrating the SIMCAD method and 15 additional materials in the range of  $6 \leq Z_{\text{eff}} \leq 15$  for evaluating the classification performance. We show that the correction algorithm accurately reconstructs the measured attenuation curve, and thus gives higher detection rates. We show that using the spectral correction leads to an accuracy increase of 1.6 and 3.8 times in estimating  $\rho_e$  and  $Z_{\text{eff}}$ , respectively.

**Keywords:** Spectral X-ray CT, Material classification, Photon counting X-ray detector, Spectral correction, Joint reconstruction, Security screening

## 1. INTRODUCTION

X-ray radiography and Computed Tomography (CT) widely used for Non-Destructive Testing (NDT) in industrial or laboratory applications give structural images of a material, however do not typically measure material

---

Further author information: (Send correspondence to Doniyor Jumanazarov)

Doniyor Jumanazarov: E-mail: doniyor.jumanazarov@fysik.dtu.dk, Telephone: +40 785402585

Jakeoung Koo: E-mail: jakoo@dtu.dk

Henning F. Poulsen: E-mail: hfpo@fysik.dtu.dk

Ulrik L. Olsen: E-mail: ullu@dtu.dk

Mihai IOVEA: E-mail: office@accent.ro

Quantum Optics and Photon Counting 2021, edited by Ivan Prochazka, Martin Štefaňák,  
Roman Sobolewski, Aurél Gábris, Proc. of SPIE Vol. 11771, 117710J · © 2021 SPIE  
CCC code: 0277-786X/21/\$21 · doi: 10.1117/12.2589290

properties such as electron density,  $\rho_e$ , and effective atomic number,  $Z_{\text{eff}}$ .<sup>1,2</sup> The main reason is that the energy dependence of the attenuation is not measured. Security screening systems currently use dual-energy CT (DECT) for material recognition<sup>3-8</sup> with two channels of energy discrimination. However, the dual-energy CT suffer from two main limitations. Firstly, they typically use dual sandwiched energy integrating detectors leading to poor energy separation due to overlapping low- and high-energy spectrums. Secondly, the DECT only measures two different data points in the attenuation spectrum and therefore, only provide limited material classification maps. The development of cadmium telluride (CdTe) energy discriminating imaging detectors has laid groundbreaking step towards multi-energy Spectral CT (SCT) and other energy-resolved imaging modalities.<sup>9-11</sup> These detectors can discriminate the energy of the incident photons enabling the simultaneous collection of the spectrum of the whole range of material's energy-dependent linear attenuation coefficients (LACs) and provide material features. Spectral CT simultaneously measures the energy dependence of a material's LAC using energy resolved photon counting detectors (PCD). Spectral CT is proven to be superior to dual-energy CT for enhancing material recognition.<sup>12</sup> Radiography studies also showed that PCDs have clear advantages over dual-layer sandwich detectors in reducing the false detection rate.<sup>13-15</sup> The poor spectral separation in the dual-layer sandwich detectors was found to be the major reason for the lower performance. This has attracted significant attention in PCDs for material characterization within security applications.<sup>16-18</sup>

DECT Systems typically use an attenuation decomposition method presented by Alvarez et al.<sup>19</sup> for the formulation of an alternative material characterization. It decomposes a material's linear attenuation coefficient (LAC) into photoelectric absorption and Compton scattering basis functions and can define the whole spectral range of the LAC through just two parameters, density,  $\rho$ , and effective atom number,  $Z_{\text{eff}}$ . However, such material identification through the effective LAC using dual-energy sandwich detectors is a system-dependent solution, i.e. depend on source spectrum, filtration, and detector efficiency of the scanner.<sup>20</sup> Recently, Azevedo et al.<sup>21</sup> presented a method that measures ( $\rho_e$ ,  $Z_{\text{eff}}$ ) from dual-energy CT called the System-Independent  $\rho_e/Z_{\text{eff}}$  (SIRZ), independent of the scanning instrument, and Champley et al.<sup>22</sup> have improved the method further (SIRZ-2).

Busi et al.<sup>23</sup> have adopted the SIRZ method for Spectral CT with the Spectral  $\rho_e/Z_{\text{eff}}$  Estimation (SRZE) method, which measures both system-independent material features directly from the energy-dependent LACs. However, the SRZE method uses 64 energy bins for the optimal accuracy and gives significantly lower accuracy at two energy bins.

In previous work we presented a novel classification method, named system-independent material classification through attenuation decomposition (SIMCAD),<sup>24</sup> which measures the material features ( $\rho_e$ ,  $Z_{\text{eff}}$ ), independent of the instrument or specifics of the scanner such as the X-ray spectrum, directly from energy resolved LACs in spectral CT. The method uses attenuation decomposition presented by Alvarez et al.<sup>19</sup> for the formulation to adopt it for multiple energies. It was demonstrated with the experimental data that the SIMCAD method can reach the optimal classification performance with optimized bi-energy bins and can give comparable results to the SRZE method. Therefore, the SIMCAD method spends at least 32x shorter time for the tomographic reconstruction after the data acquisition due to a lower number of energy bins used. The speed enables the method well suited for the requirements of rapid scanning for real applications such as check-in baggage control at airports.<sup>25</sup> It is worth noting that even if SIMCAD only used two bins and thus had the same number of data points of the energy spectrum as DECT, the overlap in DECT energy bins does not exist for PCD systems which leads to the improved performance. The above classification methods rely on accurate LAC curves. However, detector effects, such as charge sharing and pulse pileup, strongly distort the measured spectrum of photon-counting x-ray detectors operating under high flux.<sup>26</sup> These effects lead to severe deviation between the measured and the transmitted spectrum, and therefore to a significant decrease in material identification performance when used for both security and industrial applications. Thus, the correction of the detector's spectral response is required to correct the measured LACs. To correct for these distortions, we use a correction algorithm developed by Dreier et al.<sup>27</sup> This is a comprehensive semianalytical correction algorithm that corrects the raw data distorted by charge sharing, weighting potential, pulse pileup, incomplete charge collection, and x-ray fluorescence based on spectral distortion models. With small correction the correction algorithm is could be applied to any photon counting CdTe detector. In this work, we scan 35 different materials with 12 projections and reconstruct using the joint reconstruction method VTV. We analyze the contribution of the correction

algorithm in material identification from sparse (few projections) Spectral CT, because the spectral correction requires additional computation time which is a key factor for security and industrial applications.

## 2. EXPERIMENTAL SETUP AND MATERIALS. DATA CORRECTION ALGORITHM

In this section, we define the system-independent physical properties used to classify materials and LACs. We then present the experimental setup and the samples used to conduct the experiments. Lastly, the detector, data correction and sinogram generation are introduced.

### 2.1 Physical properties of materials

Linear attenuation coefficient (LAC) is proportionally dependent upon a material's electron density.<sup>28</sup> The electron density is the number of electrons per unit volume (electron – mole/cm<sup>3</sup>). For a compound or mixture that consists of  $N$  total different elements, the electron density can be expressed as

$$\rho_e = \frac{\sum_{i=1}^N \alpha_i Z_i}{\sum_{i=1}^N \alpha_i A_i} \rho. \quad (1)$$

where  $\rho$  is mass density (g/cm<sup>3</sup>),  $A_i$  and  $Z_i$  are atomic mass and atomic number for each element,  $i$ , respectively,  $\alpha_i$  is the number of atoms that have atomic number  $Z_i$ . For compounds, the atomic number is referred to as effective atomic number,  $Z_{\text{eff}}$ , which can be classically parameterized as<sup>29,30</sup>

$$Z_{\text{eff}} = \sqrt[l]{\sum_{i=1}^N r_i Z_i^l}, \quad (2)$$

where  $r_i$  is “relative electron fraction” contribution of an element,  $i$ ,

$$r_i = \frac{\alpha_i Z_i}{\sum_{j=1}^N \alpha_j Z_j},$$

In previous work,<sup>24</sup> the exponent  $l$  was studied to optimize the value for the best classification performance for the materials, source spectrum and system features used. The value of  $l = 8.0$  showed the highest accuracy, thus we choose this value for the calculations of reference  $Z_{\text{eff}}$  values in this work.

### 2.2 Decomposition of LAC

For a computed tomography system, Alvarez et al.<sup>19</sup> presented empirically over the range of 30–200 keV that the LAC could be decomposed in the form:

$$\mu(E) = a_1 \frac{1}{E^3} + a_2 f_{\text{KN}}(E), \quad (3)$$

where  $f_{\text{KN}}(E)$  is the Klein-Nishina function

$$f_{\text{KN}}(\varepsilon) = \frac{1 + \varepsilon}{\varepsilon^2} \left( 2 \frac{1 + \varepsilon}{1 + 2\varepsilon} - \frac{\ln(1 + 2\varepsilon)}{\varepsilon} \right) + \frac{\ln(1 + 2\varepsilon)}{2\varepsilon} - \frac{1 + 3\varepsilon}{(1 + 2\varepsilon)^2}, \quad (4)$$

and  $\varepsilon = E/511$  keV ( $\varepsilon = E/m_e c^2$ ) is the reduced energy of the incident photon. The functions  $1/E^3$  and  $f_{\text{KN}}(E)$  represent approximation of the energy dependence of the photoelectric absorption and Compton scattering, respectively. With exception of the absorption edges effect, they further presented that the photoelectric coefficient,  $a_1$  and the Compton scattering coefficient,  $a_2$  could be defined as:

$$a_1 \approx K_1 \frac{\rho}{A} Z^n, \quad a_2 \approx K_2 \frac{\rho}{A} Z \quad (5)$$

where  $K_1$  and  $K_2$  are constants,  $\rho$  is mass density ( $\text{g}/\text{cm}^3$ ),  $A$  is atomic mass and  $Z$  is atomic number.  $n$  is the exponent for photoelectric attenuation (per atom).  $n$  is optimized for each of the classification approaches depending on how many energy bins are used.  $a_1$  and  $a_2$  are expressed with approximation. The insertion of  $a_1$  and  $a_2$  from Eq. 5 into Eq. 3 gives the LAC as:

$$\mu(E) = \frac{Z}{A} \rho (Z^{n-1} p(E) + c(E)), \quad (6)$$

where

$$p(E) = K_1 \frac{1}{E^3}, \quad c(E) = K_2 f_{\text{KN}}(E). \quad (7)$$

$p(E)$  and  $c(E)$  are photoelectric absorption and Compton scattering basis functions, respectively. Inserting Eq. 1 into Eq. 6 we retrieve a parameterized LAC for a compound as

$$\mu(E) = \rho_e (Z_{\text{eff}}^{n-1} p(E) + c(E)). \quad (8)$$

The basis functions are empirically measured through fitting experimental data. In this work, the basis functions and exponent  $n$  are calibrated to retrieve material properties, which is discussed in the next subsection.

### 2.3 Experimental setup and materials

The experiments were conducted in the 3D Imaging Center at DTU, Denmark. The X-ray beam was generated by a Hamamatsu source working under the acceleration voltage and the filament current set to 160 kV and 0.5 mA, respectively. The focal spot is  $75 \mu\text{m}$ . An aluminum filter of 2 mm thickness was mounted after the source to suppress photons with energies lower than the detector energy range. The beam was collimated to a fanbeam using a JJ X-ray IB-80-Air to a height of 0.6mm. Directly in front of the detector a custom built 5mm thick tungsten slit (opening: 0.6mm) minimize photon scattering. The sample was placed on the rotation stage and scanned between discrete rotations with  $30^\circ$  increments over a range of 360 degrees. The source to detector distance (SDD) was set equal to 701 mm whereas the source to sample distance (SOD) was 500 mm. For material classification presented in the subsection 5.3, the total integration time per projection was set to 8 seconds.

The sample scanned for the uses in the subsections 5.1 and 5.2 contains aluminum, magnesium and polyetheretherketone (PEEK) plastic and was scanned with different total integration time per projection varying from 2 ms to 100 ms. This sample is described in Ref. 31. Tab. 1 and Tab. 2 in Appendix A lists the materials used for the calibration as reference materials and estimation of material features, respectively. The tables include the materials' reference  $\rho_e$  and  $Z_{\text{eff}}$  values that were calculated by using Eq. 1 and Eq. 2 respectively. Sample dimension are also presented through width $\times$ length for rectangular samples or diameter for circular samples. The plastics shown in the tables are polymethyl methacrylate (PMMA), polytetrafluoroethylene (PTFE), polyvinylidene fluoride (PVDF), polycarbonate (PC), polyoxymethylene-C (POM-C), polyethylene terephthalate (PET) and polyoxymethylene-H (POM-H). Materials used are commonly found in checked-in luggage, and explosive or precursor materials without K-edge absorption within the detector's energy range and in the range of  $6 \leq Z_{\text{eff}} \leq 15$ .

### 2.4 The detector and data correction for spectral distortion

The detector adopted for the current experiments is MultiX ME-100 v2 manufactured by Detection Technology S.A.S. in Moirans, France. We use a system of five detector modules, each module has a  $1 \times 128$  linear array of pixels sized  $0.8 \times 0.8 \text{ mm}^2$ . The number of energy bins is 128 with a width of 1.1 keV each, evenly distributed in the energy range between 20 and 160 keV. The energy resolution of the detector operating at high X-ray fluxes is 6.5% (8 keV at 122 keV).<sup>11</sup> The detector has a CdTe sensor with 3 mm thickness. Incident photons strike a collective cathode being composed of a continuous metal film. The sensor has pixelated anodes with significantly smaller size, which are located on readout electronics.

The spectral response of photon counting detectors is severely distorted by a range of physical effects occurring inside CdTe sensor crystal. These energy and flux dependent effects decrease the energy resolution of PCDs and induce distortion in measured LAC curves. A X-ray photon absorbed near a pixel border generates electron

charge cloud which may split between neighboring detector pixels. As a result, the high-energy x-ray photon is falsely counted as two photons which have lower energies. This physical phenomenon is called charge sharing. Another phenomenon is related to X-ray fluorescence. Detector sensor materials Cd and Te present K-edges at 26.7 keV and 31.8 keV, respectively. Incoming x-rays at an energy  $E$  can expel K-electrons of CdTe sensor crystal when the photon energy is larger compared to the K-shell binding energies. The vacant K-shells are instantly reoccupied, and the fluorescence K-shell X-ray photons with energy  $E_{\text{fl}}$  are emitted and are in some cases re-absorbed and registered in the detector pixel itself or in adjacent detector pixels (K-escape). As a result, the incoming photons are registered at an energy  $E - E_{\text{fl}}$ , and the consequent peak in the energy spectrum is called K-escape peak. Thus, high-energy x-rays are again recorded at lower energies which leads to a decrease in energy separation and also spatial resolution.

Charge sharing and K-escape are border interactions. Contribution of these phenomena to the overall detector response decreases as the size of the detector pixels increases, which can lead to improved energy discrimination. However, the number of incident X-ray photons striking the same pixel increases in time if the pixel has larger size. This may result in the overlapping of pulses created by two photons, which may be recorded as one photon at a very high energy. This effect is called pulse pile-up. Pulse pile-up can cause non-linear detector counting statistics and eventually detector saturation.<sup>32</sup> The contribution of this effect to the total detector response can be reduced with designing smaller pixels, however, this may result in increased charge sharing and K-escape. Discovering the best size of the detector pixels to steady charge sharing, K-escape and pulse pile-up is very important in making a PCD.

Charge carriers that are counted by one detector pixel may again produce a pulse in the adjacent pixel. This phenomenon is called weighting potential (WP) cross talk and gives rise to the source spectrum at energies lower than 30 keV.<sup>27</sup> Effects such as electronic noise<sup>33</sup> and Compton scattering of the incoming photons in the detector crystal are another problems of PCDs. Both effects have less contributions to the detector signal compared to other effects.

CdTe detectors are also subjected to another challenge that is charge trapping. Some of charge carriers are trapped in crystal lattice defects or impurities, which are non-uniformly distributed.<sup>34</sup> This results in the effect called incomplete charge collection (ICC). The ICC becomes visible in the spectrum at energies higher than 60 keV.<sup>35</sup> The electrons and holes move at drift velocities  $v_e = \mu_e E_e$  and  $v_h = \mu_h E_e$  towards the collective cathode and pixelated anodes, respectively.  $\mu_e$  and  $\mu_h$  are the electron and hole drift mobilities, respectively, and  $E_e$  is the external electric field. The holes drift with significantly smaller mobility than electrons. The electrons have 1000 cm<sup>2</sup>/V of the drift mobility whereas the holes have 80 cm<sup>2</sup>/V.<sup>36</sup> This leads to more severe trapping of the slow holes than electrons. The hole trapping is typically reduced by designing CdTe detector with much smaller pixelated anodes than the crystal thickness. This gives comparatively far less contribution of hole transport to the total signal and, thus, reduces ICC effect.<sup>37</sup> Moreover, the trapped holes create the accumulation of positive charges in the crystal which can change the external electric field distribution over time and distort the characteristics of the charge collection. This effect is called polarization and also can lead to ICC.<sup>34,38</sup> Polarization might cause noticeable ring artifacts in the reconstructed images at higher photon fluxes,<sup>32</sup> and also rapid decrease in signal pulses above a definite high flux rate.<sup>39</sup>

In the correction algorithm, using the simulated detector response matrix the distorted spectrum is first corrected for the flux-independent effects, such as charge sharing, WP cross talk, X-ray fluorescence (escape peaks), Compton scattering and electronic noise. Flux-independent effects are corrected by using an inverse detector response matrix  $\mathbf{M}_C$  of size  $N \times N$ , where  $N$  is the number of energy bins. The raw data is represented as matrix  $\mathbf{I}_R$  of size  $N \times J$ , where  $J$  is the number of detector pixels. The matrix for corrected data for each pixel is obtained by<sup>27</sup>

$$\mathbf{I}_C = \mathbf{M}_C \mathbf{I}_R, \quad (9)$$

The inverse detector response matrix is decomposed into the individual detector response matrices, and it is computed as<sup>27</sup>

$$\mathbf{M}_C = \mathbf{D}_{\text{WP}} \mathbf{D}_E \mathbf{D}_C, \quad (10)$$

where  $\mathbf{D}_{\text{WP}}$ ,  $\mathbf{D}_E$  and  $\mathbf{D}_C$  are the detector response matrices corresponding to WP cross talk, Compton scattering and electronic noise, and charge sharing effects, respectively. The WP cross talk is firstly calculated to correct distortion at low energies. The charge sharing is lastly corrected.

For each pixel's response to X-ray illumination, a Monte Carlo simulation is employed to calculate the total detector response matrix, which is dependent on the incident X-ray energy and location of photon's energy deposition. The location of photon absorption is considered as a function of depth in the sensor under the probability distribution function defined by the reference LACs which are obtained from NIST cross-sections.<sup>40</sup> In the simulation, the escape peaks phenomenon occurring due to X-ray fluorescence is firstly defined, by assuming that the emitted fluorescence photons are directed randomly and absorbed at certain travel distance.  $\mathbf{D}_{WP}$ ,  $\mathbf{D}_E$  and  $\mathbf{D}_C$  detector response matrices are then computed separately based on 2-D histograms of registered and actual incident energy of X-rays in the simulation. In the model of calculating charge sharing, the excited electron cloud is split between two adjacent pixels based on a 1-D Gaussian distribution that is aligned with the detector array. The excited charge cloud can induce current in the adjacent pixels, and the amount of WP cross talk is proportional to the amount of current. A simplified model presented in Ref. 41 is used for calculating WP cross talk, in which the detector is considered as the detector surfaces are composed of two infinite parallel sheets. The model employs the approach of reflected dipole layers (mirror charges), which assumes that WP cross talk is defined as an infinite sum of the WP elementary functions corresponding to the reflected dipole layers distributed at equal distances dependent on the depth of the crystal.

Flux dependent models such as the pulse pileup and incomplete charge collection are then considered for correction. The model presented by Plagnard<sup>42</sup> is employed to correct for the pile-up phenomenon. The pile-up effect of photon with energy  $E_n$  on other whole energies  $E_x$  of the measured spectrum  $I_R(E)$  gives the respective pile-up spectrum  $I_P(E_{nx})$ , which is defined for all the range of  $x$  as<sup>27,42</sup>

$$E_{nx} = E_n + E_x, \quad (11)$$

$$I_P(E_{nx}) = \frac{I_R(E_n)}{I_R(E)_{\max}} C_P I_R(E_x). \quad (12)$$

It is assumed that the two photons with energies  $E_n$  and  $E_x$  in the measured spectrum are recorded as one photon with energy  $E_{nx}$  in the pile-up spectrum.  $C_P$  is a coefficient for defining pile-up probability. Dreier et al.<sup>27</sup> uses an automatic fitting method to compute this coefficient using the spectral LACs of aluminum. The pile-up spectrum is deducted from the measured spectrum, and the result is added to  $\sum_x I_P(E_{nx})$  summed over the whole range of  $x$ . This gives the corrected spectrum  $I_C(E_n)$  of the energy bin  $n$ <sup>27</sup>

$$I_C(E) = I_R(E) - I_P(E), \quad (13)$$

$$I_C(E_n) = I_C(E_n) + \sum_x I_P(E_{nx}). \quad (14)$$

To obtain the whole corrected spectrum, the same modelling is applied for each increment of  $n$  changing from the initial to final values. We refer the reader to Dreier et al.<sup>27</sup> for more details of the correction algorithm.

## 2.5 Sinogram generation

The correction of the raw data is followed by converting the photon counts to line integral or sinogram for each energy bin based on Lambert–Beer's law as follows:

$$L_k(\vec{x}) = -\log \frac{I_k(\vec{x})}{I_{0,k}(\vec{x})}, \quad k = 1, 2, 3, \dots, 128; \quad (15)$$

where  $I_{0,k}$  is the flat-field photon flux corresponding to energy bin  $k$  measured without the sample,  $I_k$  is the measured photon flux for energy bin  $k$  that has passed through the material,  $\vec{x}$  is the 1D detector pixel array.

## 3. IMAGE RECONSTRUCTION METHOD AND LAC EXTRACTION

In this section, we briefly describe the joint reconstruction method we previously presented in Ref.<sup>31</sup> We also present how LAC is extracted, and the data is rebinned into 2 and 15 energy bins between low- and high-energy thresholds. Lastly, we present a tool for analyzing the reconstructed image quality obtained for the raw and corrected data.

### 3.1 Joint reconstruction

In Spectral CT, we measure a stack of energy-resolved sinograms with  $N$  energy bins denoted by  $\mathbf{p}_1, \dots, \mathbf{p}_N \in \mathbb{R}^M$ , with  $M$  being the number of detector pixels multiplied by the number of projection angles. From the spectral sinograms, we target to reconstruct  $N$  respective images of  $\mathbf{u}_1, \dots, \mathbf{u}_N \in \mathbb{R}^J$  for each energy bin  $E_i$ , with  $J$  being the number of pixels for each image. Energy-resolved LACs are retrieved directly from these spectral reconstructions. We denote a stack of spectral sinograms by a vector  $\mathbf{p} \in \mathbb{R}^{NM}$  and a stack of  $N$  reconstructions by  $\mathbf{u} \in \mathbb{R}^{NJ}$  as well as the LAC for the energy bin  $E_i$  on the  $j$ -th pixel by  $u_{i,j}$ .

An operator, known as the forward projection, maps the images onto the sinogram domain and the forward-projection is commonly formulated as a linear operator  $\mathbf{A}$  such that  $\mathbf{A}\mathbf{u} = \mathbf{p}$ . Here, we use the same forward-projection operator for each energy bin and  $\mathbf{A}$  is the stack of such operators. This formulation enables comparing the estimation with the sinogram data  $\mathbf{p}$  and we want to minimize the reprojection error (distinction between the synthesized and observed sinogram) in  $L_2$  norm as follows:

$$\mathcal{G}(\mathbf{A}\mathbf{u}) = \frac{1}{2} \|\mathbf{A}\mathbf{u} - \mathbf{p}\|_2^2. \quad (16)$$

To deal with noisy data and a small number of projection angles and obtain better reconstruction taking advantage of multi-spectral dimensionality of reconstructions, we consider a regularization term by imposing a prior knowledge on the solutions. We employ a vectorial total variation scheme called  $L_\infty$ -VTV, which correlates the image gradients using maximum norm over multi energy bins as follows:

$$\mathcal{R}_{\text{VTV}}^{L_\infty}(\mathbf{u}) := \sum_{j=1}^J \left( \max_{1 \leq i \leq N} |\nabla_x u_{i,j}| + \max_{1 \leq i \leq N} |\nabla_y u_{i,j}| \right), \quad (17)$$

where  $u_{i,j}$  represents the image value for  $i$ -th energy bin and  $j$ -th pixel and  $\nabla_x$  and  $\nabla_y$  the gradient operators with respect to  $x$  and  $y$  axis, respectively. We found in our previous work<sup>31</sup> that this  $L_\infty$ -VTV norm correlates the gradients strongly over spectral dimension, rejecting outliers in gradient magnitudes.

We aim to minimize the sum of the data fitting term (Eq. 16) and the regularization term (Eq. 17) with a weighting parameter  $\lambda$  between two terms as follows:

$$\min_{\mathbf{u} \geq 0} \lambda \mathcal{G}(\mathbf{A}\mathbf{u}) + \mathcal{R}_{\text{VTV}}^{L_\infty}(\mathbf{u}), \quad (18)$$

where a non-negativity constraint is imposed on  $\mathbf{u}$  such that the LAC values should be non-negative. We refer to Jumanazarov et al.<sup>31</sup> for details of the optimization of our objective function defined in Eq. 18, and stopping criteria for the number of iterations.

### 3.2 LAC extraction

After energy resolved reconstruction and manual segmentation, for each material and each energy bin the LAC value of a segment is calculated from attenuation value histogram based on normal distribution fitting method within a region of interest (ROI) of a sample.<sup>24</sup> Fig. 1 presents an example of magnesium's spectral LAC calculated both from the raw data and from the data corrected using the correction algorithm as described in the subsection 2.4. the two experimental curves are compared to the reference curve of LAC. The correction algorithm largely restores the LAC towards the reference curve at the low energies, however, fails to correct for additional spectral distortions at lower and higher energies. One reason for this could be because of detector flux variation and photon starvation, i.e. complete attenuation of photons.<sup>27</sup> Energy bins in which the LAC is deviating from the reference values even after applying the correction algorithm are excluded in the later processing by placing low- and high-energy thresholds,  $E_l$  and  $E_h$ .

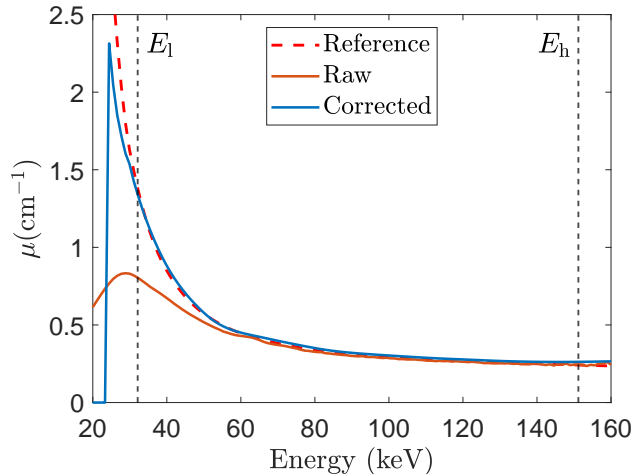


Figure 1: Spectral LAC for magnesium obtained from the raw and corrected data. The reference LACs were obtained by employing NIST cross-sections.<sup>40</sup> The vertical black dash-dotted lines represent the low- and high-energy thresholds,  $E_l$  and  $E_h$  remaining same for all materials estimated.

### 3.3 Rebinning energy bins

In this work, we test the classification performance with approaches using 2 and 15 energy bins, rebinning the corrected data by integrating photon counts between low- (33.2 keV) and high-energy (131.3 keV) thresholds. Each bin in 15 energy bins approach has equal width. The 2 bin approach has a gap between low- and high-energies, which corresponds to interval between 63.0 keV and 79.5 keV. To separate it from a simple rebinning into two bins we refer to it as a bi-energy approach in the remainder of the article. 15 energy bins provide high resolution spectral reconstruction with energy bin widths (6.6 keV) below the detector energy resolution (8 keV) and give measurement of spectral LAC curve of the raw and corrected data, however, spectral distortion of attenuation curve for the raw data is more visible in this approach. With only two energy bins the bi-energy approach are less sensitive to detector artefacts furthermore it integrates more photons into each of the two bins, and consequently are robust to significantly higher noise levels. Finally reconstructing only 2 energy bins makes this approach more computationally efficient. In our previous work,<sup>24</sup> we found that the approaches with energy bin widths below the detector energy resolution did not lead to noticeable improvement in classification performance. Still Spectral CT has a trade-off between spectral binning and noise level and moreover, to match industrial fast scanning application we only use 12 projections. Both aspects may result in more reconstruction artifacts and to compensate for these aspects, we use the joint reconstruction method,  $L_\infty$ -VTV, described in the subsection 3.1. The classification results are presented in the subsection 5.3.

### 3.4 Tool for evaluation of reconstruction quality

We use a correlation coefficient as a tool to measure the quality of reconstruction  $\mathbf{u}$  determining the extent of linear relation to the ground-truth image  $\mathbf{v}$ , defined as

$$r = \frac{\sum_i (u_i - \bar{u})(v_i - \bar{v})}{\sqrt{\sum_i (u_i - \bar{u})^2 \sum_i (v_i - \bar{v})^2}}, \quad (19)$$

where  $\bar{u}$  and  $\bar{v}$  are the mean values, and  $u_i$  and  $v_i$  represent the  $i^{\text{th}}$  pixel values of  $\mathbf{u}$  and  $\mathbf{v}$ , respectively.

We also investigate the L-curve criteria<sup>43,44</sup> on both raw and corrected data. The L-curve criteria is a plot of the 2-norm of maximum gradients,  $\|\mathbf{u}_\lambda\|_{L_\infty\text{-VTV}}$  (Eq. 17), as a function of the 2-norm of the corresponding residual vector,  $\|\mathbf{A}\mathbf{u}_\lambda - \mathbf{p}\|_2$  (Eq. 16), both dependent on weighting parameters. Based on the L-curve, one can find the optimal weighting parameter for a regularized reconstruction method without the ground truth image of a sample. Ideally, the plot appears L-shaped, and the weighting parameters  $\lambda$  corresponding to the point exactly at the knee of the curve represents the optimal  $\lambda$  values. The values on the flat and vertical lines result in over-regularized and under-regularized solutions, respectively. Therefore, when studying a real experimental

sample this graphical tool can be used to find the optimal  $\lambda$  values without using the ground truth image. We use a linear-linear scale for plotting as in Refs. 31,44. In our previous work,<sup>31</sup> we found the optimal  $\lambda$  value for the corrected data based on the L-curve criterion. In this work, we study how this graphical tool works for the raw data.

We found in our study that using the minimization of the standard deviation within a ROI of a sample as a method to find the optimal weighting parameter  $\lambda$  may lead to over-regularization. We therefore excluded it from estimation of reconstruction quality.

#### 4. METHOD TO MATERIAL CLASSIFICATION

In this section, we briefly give a description of the SIMCAD method presented in detail by Jumanazarov et al.<sup>24</sup> to measure  $\rho_e$  and  $Z_{\text{eff}}$  of materials from Spectral CT.

##### 4.1 Calibration of parameters in LAC

From Eq. 8, LAC for each energy bin can be represented as

$$\mu_m(E_k) = \rho_{e,m} \left( Z_{\text{eff},m}^{n-1} p(E_k) + c(E_k) \right), \quad (20)$$

where  $m = 1, 2, \dots, M$ ,  $k = 1, 2, \dots, K$  with  $M$  being the total number of reference materials and  $K$  being the number of energy bins used for a particular classification approach.  $p(E_k)$  and  $c(E_k)$  are photoelectric absorption and Compton scattering basis functions for energy bin  $E_k$ , respectively, which are calibrated and the same for all materials.

We also optimize the exponent  $n$  together with the basis functions for better measurement. To solve Eq. 20, we set positivity constraints for all basis functions and  $n$ , and formulate the non-linear objective function as:

$$\min_{0 \leq p_1, c_1, \dots, p_K, c_K, n} \sum_{m=1}^M \sum_{k=1}^K \left( \mu_m(E_k) - \rho_{e,m} (Z_{\text{eff},m}^{n-1} p_k + c_k) \right)^2, \quad (21)$$

where  $p_k = p(E_k)$  and  $c_k = c(E_k)$ . To optimize Eq. 21, a nonlinear least square solver is used based on trust region method.<sup>45</sup> Initial constraints were chosen as  $p_k^0 = 0.5$ ,  $c_k^0 = 0.5$  and  $n^0 = 3.6$  for all  $k$ . No particular dependency on the initial constraints was observed. Note that the calibration step is independently performed for the raw and corrected data. The formulation of the classification method is compatible with an arbitrary number of energy bins.

##### 4.2 Calculation of material properties

The calibrated parameters and the measured LAC  $\mu(E_k)$  of an unknown material scanned are used to obtain  $\rho_e$  and  $Z_{\text{eff}}$ . For  $M$ - and  $K$ - total number of unknown materials and energy bins, respectively, Eq. 20 is reformulated as a linear system equation as follows:

$$\begin{pmatrix} \vec{p} & \vec{c} & & & \\ & & \ddots & & \\ & & & \vec{p} & \vec{c} \end{pmatrix} \begin{pmatrix} z_1 \\ \rho_{e,1} \\ \vdots \\ z_M \\ \rho_{e,M} \end{pmatrix} = \begin{pmatrix} \vec{\mu}_1 \\ \vdots \\ \vec{\mu}_M \end{pmatrix} \quad (22)$$

where  $z_m$  is a temporary variable introduced instead of  $\rho_{e,m} Z_{\text{eff}}^{n-1}$  and  $\vec{p} = (p_1, \dots, p_K)^T$ ,  $\vec{c} = (c_1, \dots, c_K)^T$  and  $\vec{\mu}_m = (\mu_m(E_1), \dots, \mu_m(E_K))^T$ . The size of the linear matrix in the above equation is  $(M \times K)$ -by- $(2 \times M)$  and the number of unknowns is  $2 \times M$ . With the positivity constraint on the solution we retrieve the vector  $(z_1, \rho_{e,1}, \dots, z_M, \rho_{e,M})$  that minimizes the norm in the linear least square problem. The effective atomic numbers are then obtained for all materials by

$$Z_m = \left( \frac{z_m}{\rho_{e,m}} \right)^{\frac{1}{n-1}}. \quad (23)$$

The classification accuracy was measured as the percent relative deviation from the reference values of  $\rho_e$  and  $Z_{\text{eff}}$  as follows:

$$\Delta Z_{\text{eff}}^{\text{rel}} = 100\% \cdot \frac{Z_{\text{eff}}^{\text{est}} - Z_{\text{eff}}^{\text{ref}}}{Z_{\text{eff}}^{\text{ref}}}, \quad (24)$$

$$\Delta \rho_e^{\text{rel}} = 100\% \cdot \frac{\rho_e^{\text{est}} - \rho_e^{\text{ref}}}{\rho_e^{\text{ref}}} \quad (25)$$

where superscripts est and ref represent the estimated and reference values, respectively.

## 5. RESULTS AND DISCUSSIONS

### 5.1 Correlation coefficient and L-curve

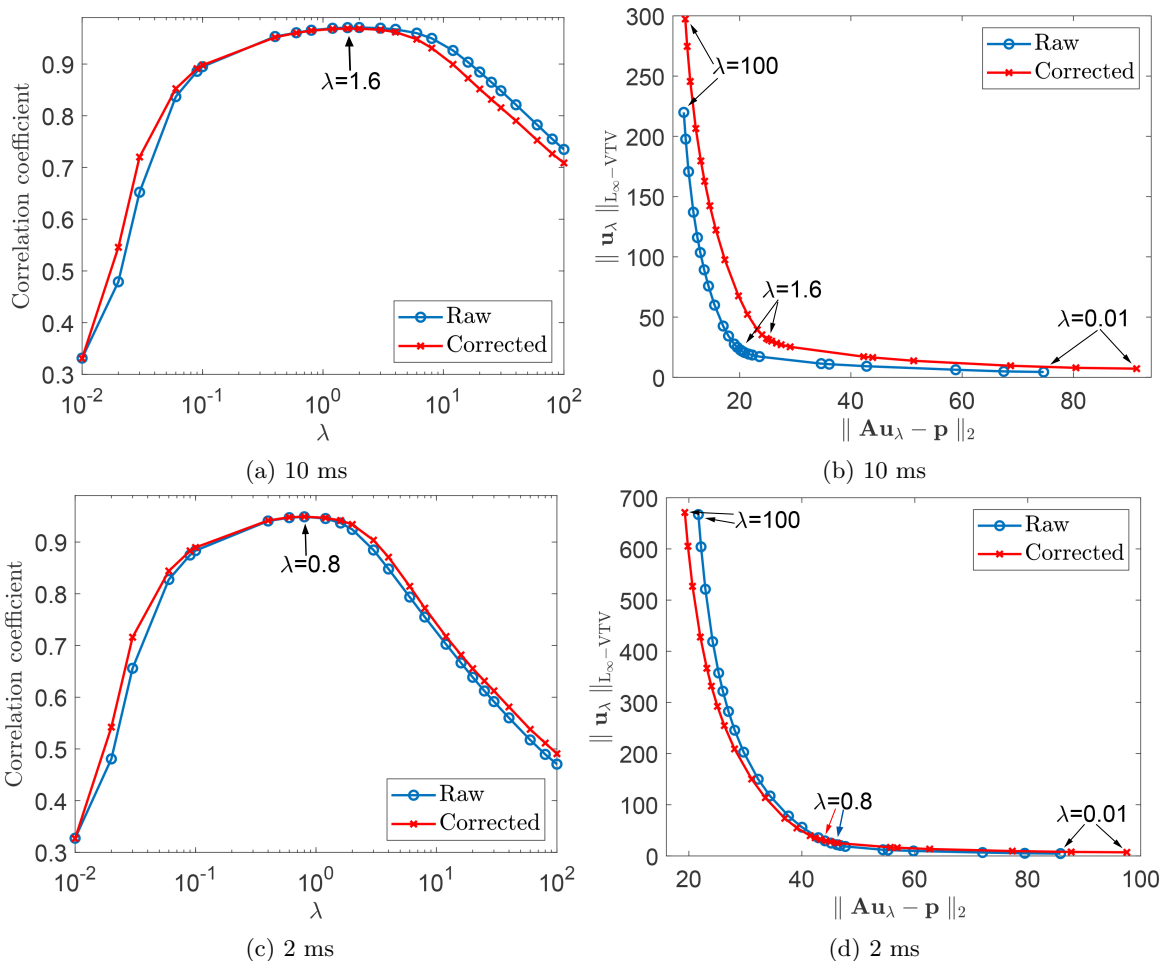


Figure 2: Correlation coefficient as a function of weighting parameter  $\lambda$  (left column) and the L-curves (right column) obtained with the raw and corrected data for 10 ms and 2 ms of integration time. The correlation coefficients represent the mean values calculated from the coefficients for 15 energy bins used. Note the logarithmic scale in the x-axis for correlation coefficients.

The sample for the experiments in this subsection was scanned with 4 different integration times 2 ms, 10 ms, 50 ms and 100 ms. The lower integration time, the lower photon counts. Fig. 2 shows correlation coefficients depending on weighting parameters and L-curve obtained with the raw and corrected data for 10 ms and 2 ms integration time. Based on the correlation coefficients the raw data have similar reconstruction quality as the

corrected data, even with noticeably deviations in the LAC as shown in Fig. 1. For all of total integration times we obtained similar correlation coefficients from the raw and the corrected data. For 10 ms acquisition time, the figure also shows good agreement between the weighting parameter found on the corner of the L-curve and the weighting parameter corresponding to the maximum correlation coefficient. We found that for both the raw and corrected data the vertical parts of the L-curves deviate from initial vertical positions as the total integration time decreases from 100 ms to 2 ms, which was more noticeable in 2 ms case. The raw data with less deflection of vertical lines appears to be slightly more accurate in fitting using the L-curve criterion compared to the corrected data.

### 5.2 Introducing high noise levels to specific energy bins

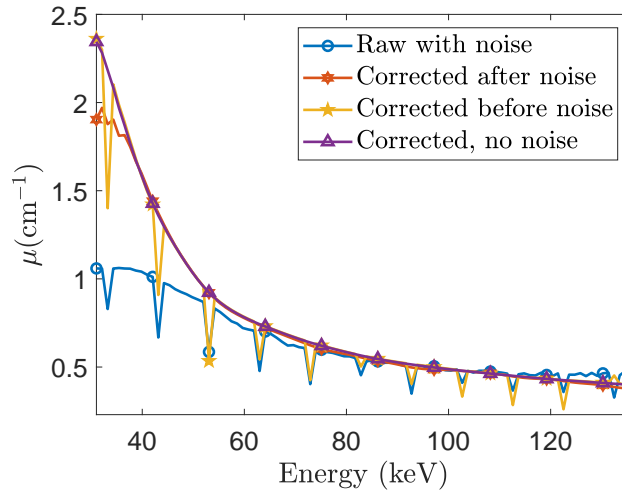


Figure 3: Spectral LAC for aluminum obtained with four different cases of adding high Gaussian noise ( $\sigma = 1.5$ ) to 11 energy bins between the low- and high-energy thresholds; noise is added to the raw data, the correction is performed after and before adding noise, and the correction is performed without adding noise.

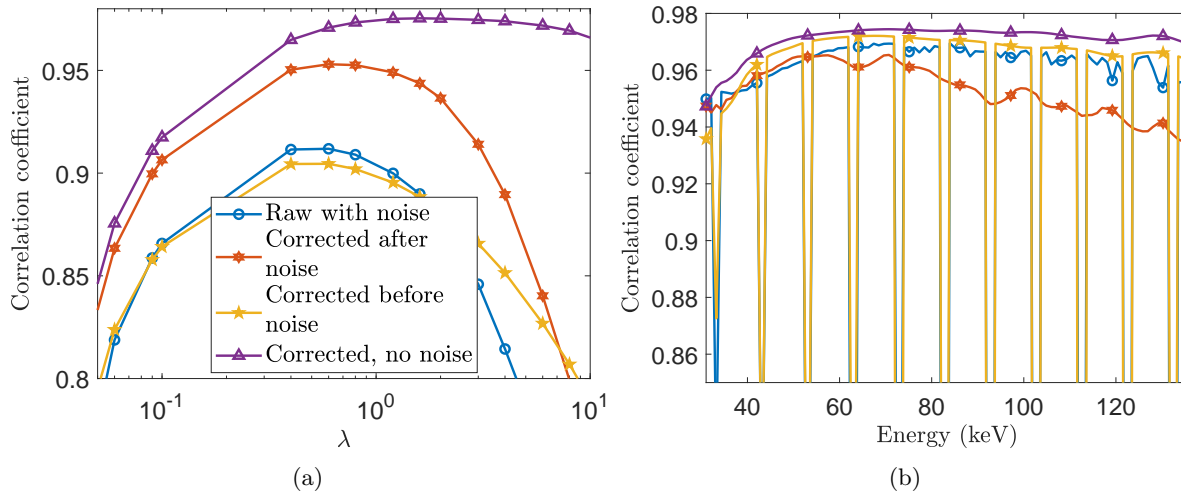


Figure 4: Correlation coefficient as a function of weighting parameter  $\lambda$  (a) and the photon energy between the low- and high-energy thresholds (b) obtained with four such different cases. The correlation coefficients (a) represent the mean values calculated from the coefficients for 96 energy bins used between the low- and high-energy thresholds. Note the logarithmic scale in the x-axis for correlation coefficients (a).

The aim of the joint reconstruction is to correlate intensity shift across the spectral dimensions such that noise in one energy bin blurring a specific edge is corrected by the information in the other channels of the same edge.

The correction algorithm redistributes intensity between energy channels based on the detector response and noise in one channel is thus distributed across the spectrum. We aimed to check the robustness of the combined workflow of correction and reconstruction to this type of noise. Gaussian noise with a standard deviation ( $\sigma$ ) of 1.5 was introduced to 11 energy bins distributed uniformly between 33.2 keV and 132.4 keV. The sample used in this subsection was scanned with 100 ms of the total integration time per projection. We investigated four different cases of added noise; noise is added to the raw data (Raw with noise), noise is added to the raw data and then the data is corrected (Corrected after noise), the raw data is corrected and then noise is added to the data (Corrected before noise) and the raw data is corrected and no noise is added (Corrected, no noise). For all cases sinograms are calculated from the data, reconstructed and manually segmented. Fig. 3 shows energy-resolved LACs from an aluminum segment for each of the 4 cases of added noise. The correction algorithm appears to largely overcome such high noises except it shows some decrease in spectral LAC in the low energy. Adding noise after the spectral correction gives noticeable drops in LACs for the affected energy bins similarly to the case of adding noise to the raw data. Fig. 4 presents correlation coefficients depending on weighting parameter  $\lambda$  and photon energy corresponding to the optimal  $\lambda$  for four such cases. It can be noted from Fig. 4a that the case of correcting before adding noise ( $r = 0.90$  at  $\lambda = 0.6$ ) even gives slightly smaller correlation coefficients compared to the case of noisy raw data ( $r = 0.91$  at  $\lambda = 0.6$ ). The correction algorithm significantly increases reconstruction quality ( $r = 0.95$  at  $\lambda = 0.6$ ) whereas the correction algorithm without added noise gives  $r = 0.97$  at  $\lambda = 1.6$ . The figure also shows that the joint reconstruction method uses lower weighting parameter in the cases of added noises corresponding to increasing the regularization between energy bins. Fig. 4b shows that the correction algorithm after adding noise mostly compensates for the affected bins giving lower overall correlation coefficients whereas the cases of the noisy raw data and the data corrected before adding noise have very sharp drops for such energy bins with added noises.

### 5.3 Material classification

Fig. 5 presents classification results for the bi- and 15 energy bins approaches. Note that we used the materials listed in Tab. 1 and Tab. 2 in Appendix A for the calibration step as the reference materials and for calculation of ( $\rho_e$ ,  $Z_{\text{eff}}$ ) as unknown materials, respectively. We obtained the relative deviations for  $\rho_e$  and  $Z_{\text{eff}}$  as a function of the weighting parameter  $\lambda$  used for the reconstruction. Even though the correlation coefficients for the raw and corrected data were found to be similar as shown in Fig. 2, the corrected data in 15 energy bins approach gives 3.4% for  $\rho_e$  and 2.7% for  $Z_{\text{eff}}$  of relative deviations at  $\lambda = 16.0$  whereas the raw data results in 5.6% and 10.3% at  $\lambda = 4.0$ , respectively. The classification accuracy for the raw data in bi-energy approach was also significantly lower than the corrected data. For bi-energy bins, the relative deviations are 8.0% for  $\rho_e$  and 12.4% for  $Z_{\text{eff}}$  at  $\lambda = 2.0$  for the raw data whereas the corrected data gives 2.6% and 3.9% deviations at  $\lambda = 6.0$ . Thus, the classification accuracy relies on how the measured LAC fits our parameterized LAC defined in Eq. 20. We found that using a bin-by-bin reconstruction method significantly deteriorates classification performance for the raw data.<sup>24</sup>

We tested the robustness of the classification performance for the raw and corrected data by adding Gaussian noise with  $\sigma = 0.15$  to all energy bins and all materials used for the calibration step and calculation of materials features between the low- and high-energy thresholds. Fig. 6 shows the relative deviations for ( $\rho_e$ ,  $Z_{\text{eff}}$ ) as a function of weighting parameter. It can be noted from the graphs that applying the correction algorithm after and before adding noise to the raw data gives similar results, for which the relative deviations are 4.1% for  $\rho_e$  and 3.3% for  $Z_{\text{eff}}$  at  $\lambda = 6.0$ , and 3.8% and 4.0% at  $\lambda = 20.0$ , respectively. In comparison, the raw data with added noise leads to the deviations of 6.5% and 11.1% at  $\lambda = 2.0$ , respectively.

## 6. CONCLUSION

We explored the influence of spectral correction applied to the raw data collected by a PCD. We found the influence on the spectrally resolved LAC curve, the reconstruction quality, the L-curve and the material classification. We used the SIMCAD classification method determining system-independent material properties ( $\rho_e$ ,  $Z_{\text{eff}}$ ). The correlation coefficient were employed to measure reconstruction quality of data acquired with different levels of photon flux, acquisition time and number of bins. We have presented that decreasing the integration time and thus decreasing photon counts, the raw data gave similar correlation coefficients and L-curve properties as the

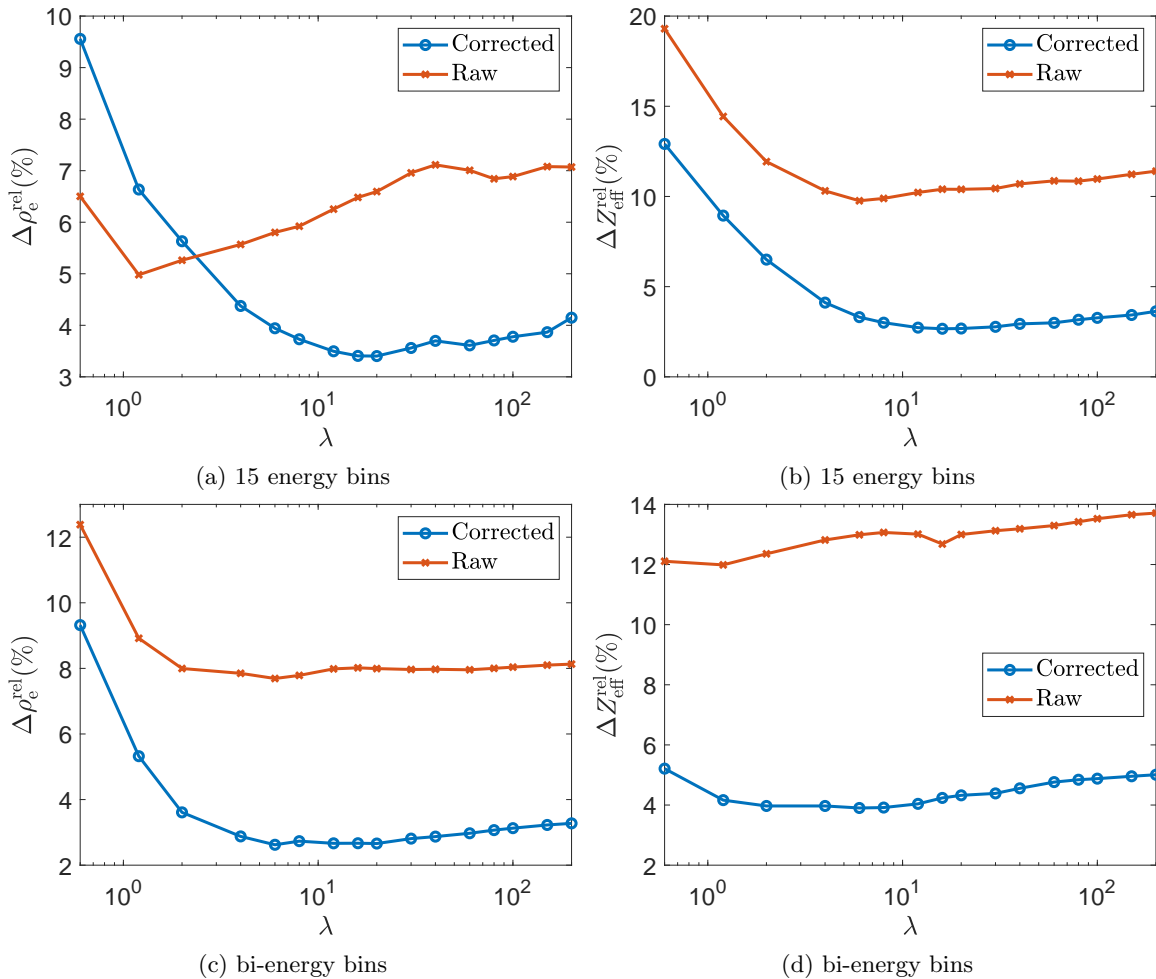


Figure 5: The percent relative deviations as a function of weighting parameter  $\lambda$  for  $\rho_e$  (left column) and  $Z_{\text{eff}}$  (right column) obtained with the raw and corrected data using bi- and 15 energy bins. The deviations are shown as the mean values of the absolute deviations for each material listed in Tab. 2. Note the logarithmic scale in the x-axis.

corrected data. However, very high noise levels introduced to certain energy bins deteriorates reconstruction quality more for the raw data than for data corrected after the noise is added. The correction algorithm showed robustness to such noise in specific energy bins in terms of correcting the noisy spectral LAC. For material classification, we investigated the influence of spectral correction both for high resolution spectral reconstruction where the number of bins exceed the energy resolution of the detector and for computational efficient binning of the spectral dimension into high and low energy bins. We also tested noise conditions for classifications with the raw and corrected data. We found that the correction algorithm significantly enhances the accuracy of the classification performance important for both security and industrial applications where materials are identified from Spectral CT. Since the spectral correction of the detector response could easily be implemented for other types of photon counting detectors, results similar to what is obtained in this study can be expected when the correction algorithm is used for other photon-counting applications and set-ups.

## APPENDIX A. MATERIALS USED FOR CLASSIFICATION

### ACKNOWLEDGMENTS

This project has received funding from the European Union Horizon 2020 research and innovation programme under the Marie Skłodowska-Curie grant agreement No. 765604 as part of the MUltiscale, Multimodal and Multidi-

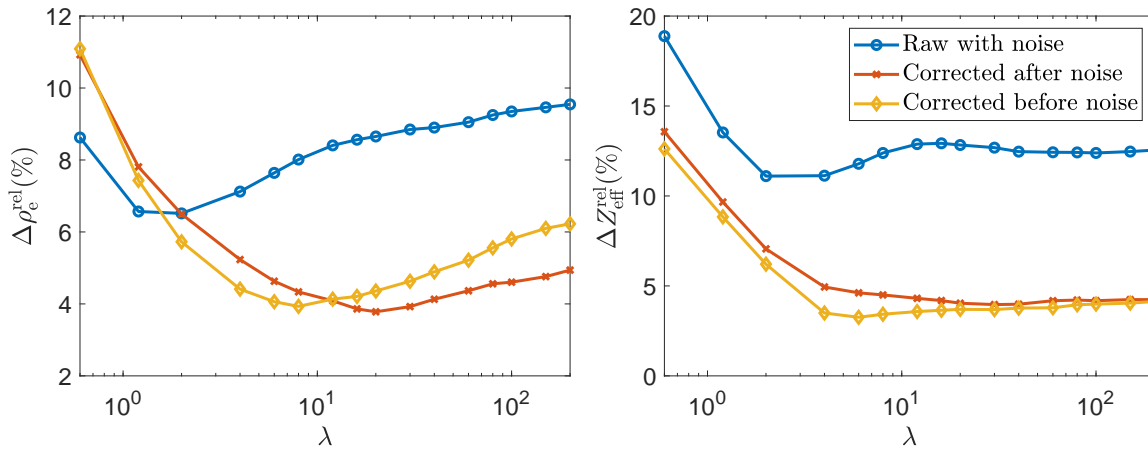


Figure 6: The relative deviations as a function of weighting parameter  $\lambda$  for  $\rho_e$  (left) and  $Z_{\text{eff}}$  (right) obtained with 15 energy bins for the 3 noise cases; noise is added to the raw data, the correction algorithm is applied after and before adding noise. The deviations are shown as the mean values of the absolute deviations for each material listed in Tab. 2. Note the logarithmic scale in the x-axis.

mensional imaging for EngineerRING project (MUMMERING Innovative Training Network, [www.mummering.eu](http://www.mummering.eu)) and from the EIC FTI program (project 853720). The authors want to acknowledge also the 3D Imaging Center at DTU, where the experiments have been conducted.

## REFERENCES

- [1] Martz, H. E., Logan, C. M., Schneberk, D. J., and Shull, P. J., [*X-ray Imaging: fundamentals, industrial techniques and applications*], CRC Press (2016).
- [2] Ying, Z., Naidu, R., and Crawford, C. R., “Dual energy computed tomography for explosive detection,” *Journal of X-Ray Science and Technology* **14**(4), 235–256 (2006).
- [3] Kalender, Willi A and Perman, WH and Vetter, JR and Klotz, E., “Evaluation of a prototype dual-energy computed tomographic apparatus. I. Phantom studies,” *Medical physics* **13**(3), 334—339 (1986).
- [4] Heismann, B. J., Leppert, J., and Stierstorfer, K., “Density and atomic number measurements with spectral x-ray attenuation method,” *Journal of Applied Physics* **94**(3), 2073–2079 (2003).
- [5] Park, J. S. and Kim, J. K., “Calculation of effective atomic number and normal density using a source weighting method in a dual Energy X-ray inspection system,” *Journal of the Korean Physical Society* **59**(4), 2709–2713 (2011).
- [6] Szczykutowicz, T. P., Qi, Z., and Chen, G.-H., “A simple image based method for obtaining electron density and atomic number in dual energy CT,” in [*Medical Imaging 2011: Physics of Medical Imaging*], **7961**, 79613A, International Society for Optics and Photonics (2011).
- [7] Semerci, O. and Miller, E. L., “A parametric level-set approach to simultaneous object identification and background reconstruction for dual-energy computed tomography,” *IEEE Transactions on Image Processing* **21**(5), 2719–2734 (2012).
- [8] Landry, G., Seco, J., Gaudreault, M., and Verhaegen, F., “Deriving effective atomic numbers from DECT based on a parameterization of the ratio of high and low linear attenuation coefficients,” *Physics in Medicine and Biology* **58**(19), 6851–6866 (2013).
- [9] Shikhaliev, P. M., “Energy-resolved computed tomography: First experimental results,” *Physics in Medicine and Biology* **53**(20), 5595–5613 (2008).
- [10] Parsai, E. I., Shvydka, D., and Kang, J., “Design and optimization of large area thin-film CdTe detector for radiation therapy imaging applications,” *Medical Physics* **37**(8), 3980–3994 (2010).
- [11] Brambilla, A., Ouvrier-Buffet, P., Rinkel, J., Gonon, G., Boudou, C., and Verger, L., “CdTe linear pixel X-ray detector with enhanced spectrometric performance for high flux X-ray imaging,” *IEEE Transactions on Nuclear Science* **59**(4 PART 3), 1552–1558 (2012).

Table 1: The list of the materials used for the calibration step as the reference materials for material classification, and their physical properties  $\rho_e$  and  $Z_{\text{eff}}$ . The mass density,  $\rho$  for the plastic materials was measured with uncertainties of  $\pm 0.15\%$ . The mass densities for the rest of materials represent the theoretical values found in PubChem data.<sup>46</sup>

Material	Chemical Formula	Width×length/ Diameter (mm)	$\rho$ (g/cm <sup>3</sup> )	$\rho_e$ (e <sup>-</sup> mol/cm <sup>3</sup> )	$Z_{\text{eff}}$
Graphite	C	12.7	1.8	0.899	6
PC	(CO <sub>3</sub> C <sub>13</sub> H <sub>8</sub> ) <sub>n</sub>	8.2×53.5	1.18	0.610	6.82
PMMA	(C <sub>5</sub> O <sub>2</sub> H <sub>8</sub> ) <sub>n</sub>	40×42	1.18	0.636	7.02
POM-C	(CH <sub>2</sub> O) <sub>n</sub>	9×53.5	1.41	0.753	7.40
PTFE	(C <sub>2</sub> F <sub>4</sub> ) <sub>n</sub>	9×53.3	2.16	1.035	8.70
N,N-Dimethylhydrazine	C <sub>2</sub> H <sub>8</sub> N <sub>2</sub>	67	0.791	0.447	6.44
Ethylenediamine	C <sub>2</sub> H <sub>8</sub> N <sub>2</sub>	67	0.90	0.509	6.44
Acetone 2	C <sub>3</sub> H <sub>6</sub> O	54	0.785	0.432	6.90
Nitrobenzene	C <sub>6</sub> H <sub>5</sub> NO <sub>2</sub>	49	1.20	0.624	7.00
Ethanol 96%	C <sub>2</sub> H <sub>6</sub> O (96%)	67×67	0.798	0.450	7.06
Methanol	CH <sub>3</sub> OH	20	0.792	0.446	7.29
Hydrazine solution	H <sub>4</sub> N <sub>2</sub> (35%)	54	1.0	0.561	7.43
Nitromethane	CH <sub>3</sub> NO <sub>2</sub>	20	1.14	0.597	7.50
Water	H <sub>2</sub> O	20	0.997	0.554	7.78
Water 3	H <sub>2</sub> O	12.7	0.997	0.554	7.78
Hyd. Peroxide 2	H <sub>2</sub> O <sub>2</sub> (50%)	73×74	1.22	0.661	7.83
Magnesium 2	Mg	18	1.74	0.859	12
Aluminum 2	Al	25	2.70	1.3	13
Aluminum 3	Al	20×20	2.70	1.3	13
Silicon	Si	25	2.33	1.161	14

- [12] Wang, X., Meier, D., Taguchi, K., Wagenaar, D. J., Patt, B. E., and Frey, E. C., “Material separation in x-ray CT with energy resolved photon-counting detectors,” *Medical Physics* **38**(3), 1534–1546 (2011).
- [13] Rinkel, J., Beldjoudi, G., Rebuffel, V., Boudou, C., Ouvrier-buffet, P., Gonon, G., Verger, L., and Brambilla, A., “Experimental Evaluation of Material Identification Methods With CdTe X-ray Spectrometric Detector,” *IEEE Transactions on Nuclear Science* **58**(5), 2371–2377 (2011).
- [14] Beldjoudi, G., Rebuffel, V., Verger, L., Kaftandjian, V., and Rinkel, J., “Multidimensional data processing methods for material discrimination using an ideal X-ray spectrometric photon counting detector,” *IEEE Transactions on Nuclear Science* **58**(6 PART 2), 3190–3203 (2011).
- [15] Beldjoudi, G., Rebuffel, V., Verger, L., Kaftandjian, V., and Rinkel, J., “An optimised method for material identification using a photon counting detector,” *Nuclear Instruments and Methods in Physics Research, Section A: Accelerators, Spectrometers, Detectors and Associated Equipment* **663**(1), 26–36 (2012).
- [16] Rebuffel, V., Rinkel, J., Tabary, J., and Verger, L., “New perspectives of X-ray techniques for explosive detection based on CdTe/CdZnTe spectrometric detectors,” in [*Proc. of the Int. Symp. on Digital Industrial Radiology and Computed Tomography*], **2**, 1–8 (2011).
- [17] Limor Martin, *Enhanced information extraction in multi-energy X-ray tomography for security*, phd thesis, Boston University (2014).

Table 2: The list of the materials used for the calculation of  $(\rho_e, Z_{\text{eff}})$  in material classification, and their physical properties  $\rho_e$  and  $Z_{\text{eff}}$ . The mass density,  $\rho$  for the plastic materials was measured with uncertainties of  $\pm 0.15\%$ . The mass densities for the rest of materials represent the theoretical values found in PubChem data.<sup>46</sup>

Material	Chemical Formula	Width×length/ Diameter (mm)	$\rho$ (g/cm <sup>3</sup> )	$\rho_e$ (e <sup>-</sup> mol/cm <sup>3</sup> )	$Z_{\text{eff}}$
PET	(C <sub>10</sub> H <sub>8</sub> O <sub>4</sub> ) <sub>n</sub>	9×53.5	1.39	0.721	7.09
POM-H	(CH <sub>2</sub> O) <sub>n</sub>	15.5×53.3	1.43	0.763	7.40
PVDF	(C <sub>2</sub> H <sub>2</sub> F <sub>2</sub> ) <sub>n</sub>	9×53.5	1.79	0.896	8.40
PTFE 2	(C <sub>2</sub> F <sub>4</sub> ) <sub>n</sub>	12.7	2.2	1.056	8.70
2-Butanone	C <sub>4</sub> H <sub>8</sub> O	83	0.805	0.447	6.76
Acetone	C <sub>3</sub> H <sub>6</sub> O	20	0.785	0.432	6.90
Methanol 2	CH <sub>3</sub> OH	81	0.792	0.446	7.29
Ethanol 40%	C <sub>2</sub> H <sub>6</sub> O (40%)	67×67	0.947	0.532	7.63
Water 2	H <sub>2</sub> O	51×51	0.997	0.554	7.78
Nitric acid	HNO <sub>3</sub> (65%)	83	1.39	0.714	7.80
Hyd. Peroxide	H <sub>2</sub> O <sub>2</sub> (50 %)	20	1.22	0.661	7.83
Magnesium	Mg	12.7	1.74	0.859	12
Aluminum	Al	25	2.70	1.3	13
Silicon powder	Si	48	0.65	0.324	14
Silicon 2	Si	12.7	2.33	1.161	14

- [18] A. Brambilla, A. Gorecki, A. Potop, C. P. and Verger, L., “Basis material decomposition method for material discrimination with a new spectrometric X-ray imaging detector,” *Journal of Instrumentation* **12**(8), P08014 (2017).
- [19] Alvarez, R. E. and Macovski, A., “Energy-selective reconstructions in X-ray computerised tomography,” *Physics in Medicine and Biology* **21**(5), 733–744 (1976).
- [20] Wells, K. and Bradley, D. A., “A Review of X-ray Explosives Detection Techniques for Checked Baggage,” *Applied Radiation and Isotopes* **70**(8), 1729–1746 (2012).
- [21] Azevedo, S. G., Martz, H. E., Aufderheide, M. B., Brown, W. D., Champley, K. M., Kallman, J. S., Roberson, G. P., Schneberk, D., Seetho, I. M., and Smith, J. A., “System-Independent Characterization of Materials Using Dual-Energy Computed Tomography,” *IEEE Transactions on Nuclear Science* **63**(1), 341–350 (2016).
- [22] Champley, K. M., Azevedo, S. G., Member, S., Seetho, I. M., Glenn, S. M., Mcmichael, L. D., Smith, J. A., Kallman, J. S., Brown, W. D., and Martz, H. E., “Method to Extract System-Independent Material Properties From Dual-Energy X-Ray CT,” *IEEE Transactions on Nuclear Science* **66**(3), 674–686 (2019).
- [23] Busi, M., Mohan, K. A., Dooraghi, A. A., Champley, K. M., Martz, H. E., and Olsen, U. L., “Method for system-independent material characterization from spectral X-ray CT,” *NDT & E International* **107**(August), 102136 (2019).
- [24] Jumanazarov, D., Koo, J., Busi, M., Poulsen, H. F., Olsen, U. L., and Iovea, M., “System-independent material classification through X-ray attenuation decomposition from spectral X-ray CT,” *NDT and E International* **116**(July), 102336 (2020).
- [25] Kheirabadi, M., BJORHOLM DAHL, A., LUND OLSEN, U., MUSTAFA, W., and LYKSBERG, M., “Multispectral x-ray CT: multivariate statistical analysis for efficient reconstruction,” in [*Developments in X-Ray Tomography XI*], **1039113**, 38, International Society for Optics and Photonics (2017).
- [26] Taguchi, K. and Iwanczyk, J. S., “Vision 20/20: Single photon counting x-ray detectors in medical imaging,” *Medical physics* **40**(10), 100901 (2013).

- [27] Dreier, E. S., Kehres, J., Khalil, M., Busi, M., Gu, Y., Feidenhans, R., and Olsen, U. L., “Spectral correction algorithm for multispectral CdTe x-ray detectors,” *Optical Engineering* **57**(5), 16 (2018).
- [28] Compton, A. H., Allison, S. K., et al., “X-rays in theory and experiment,” *New York, NY, USA: Van Nostrand* (1935).
- [29] Mayneord, WV, “The significance of the roentgen,” *Acta of the International Union Against Cancer* **2**, 271 (1937).
- [30] SPIERS, F. W., “Effective atomic number and energy absorption in tissues.,” *The British journal of radiology* **19**(218), 52–63 (1946).
- [31] Jumanazarov, D., Koo, J., Poulsen, H. F., Olsen, U. L., and Iovea, M., “Material classification from sparse spectral X-ray CT using vectorial total variation based on L infinity norm,” *Submitted to NDT & E International* (2021).
- [32] Flohr, T., Petersilka, M., Henning, A., Ulzheimer, S., Ferda, J., and Schmidt, B., “Photon-counting CT review,” *Physica Medica* **79**(October), 126–136 (2020).
- [33] Brambilla, A., Ouvrier-Buffet, P., Gonon, G., Rinkel, J., Moulin, V., Boudou, C., and Verger, L., “Fast CdTe and CdZnTe semiconductor detector arrays for spectroscopic X-ray imaging,” *IEEE Transactions on Nuclear Science* **60**(1), 408–415 (2013).
- [34] Persson, M., Huber, B., Karlsson, S., Liu, X., Chen, H., Xu, C., Yveborg, M., Bornefalk, H., and Danielsson, M., “Energy-resolved CT imaging with a photon-counting silicon-strip detector,” *Physics in Medicine and Biology* **59**(22), 6709–6727 (2014).
- [35] Eisen, Y. and Horovitz, Y., “Correction of incomplete charge collection in CdTe detectors,” *Nuclear Inst. and Methods in Physics Research, A* **353**(1-3), 60–66 (1994).
- [36] McGregor, D. S. and Hermon, H., “Room-temperature compound semiconductor radiation detectors,” *Nuclear Instruments and Methods in Physics Research, Section A: Accelerators, Spectrometers, Detectors and Associated Equipment* **395**(1), 101–124 (1997).
- [37] Barrett, H. H., Eskin, J., and Barber, H., “Charge transport in arrays of semiconductor gamma-ray detectors,” *Physical Review Letters* **75**(1), 156 (1995).
- [38] Toyama, H., Higa, A., Yamazato, M., Maehama, T., Ohno, R., and Toguchi, M., “Quantitative analysis of polarization phenomena in CdTe radiation detectors,” *Japanese Journal of Applied Physics, Part 1: Regular Papers and Short Notes and Review Papers* **45**(11), 8842–8847 (2006).
- [39] Bale, D. S. and Szeles, C., “Nature of polarization in wide-bandgap semiconductor detectors under high-flux irradiation: Application to semi-insulating Cd<sub>1-x</sub>Zn<sub>x</sub>Te,” *Physical Review B - Condensed Matter and Materials Physics* **77**(3), 1–16 (2008).
- [40] Berger, M.J., Hubbell, J.H., Seltzer, S.M., Chang, J., Coursey, J.S., Sukumar, R., Zucker, D.S., and Olsen, K., “XCOM: Photon Cross Section Database,” (2010).
- [41] Guerra, P., Santos, A., and Darambara, D. G., “Development of a simplified simulation model for performance characterization of a pixellated CdZnTe multimodality imaging system,” *Physics in Medicine and Biology* **53**(4), 1099–1113 (2008).
- [42] Plagnard, J., “Comparison of measured and calculated spectra emitted by the X-ray tube used at the Gustave Roussy radiobiological service,” *X-Ray Spectrometry* **43**(5), 298–304 (2014).
- [43] Hansen, P. C., “The L-Curve and its Use in the Numerical Treatment of Inverse Problems,” in *Computational Inverse Problems in Electrocardiology*, ed. P. Johnston, *Advances in Computational Bioengineering* **4**, 119–142 (2000).
- [44] Yang, X., Hofmann, R., Dapp, R., van de Kamp, T., Rolo, T. d. S., Xiao, X., Moosmann, J., Kashef, J., and Stotzka, R., “TV-based conjugate gradient method and discrete L-curve for few-view CT reconstruction of X-ray in vivo data,” *Optics Express* **23**(5), 5368 (2015).
- [45] Nocedal, J. and Wright, S. J., [*Numerical Optimization*], Springer, New York (1999).
- [46] Kim, S., Chen, J., Cheng, T., Gindulyte, A., He, J., He, S., Li, Q., Shoemaker, B. A., Thiessen, P. A., Yu, B., Zaslavsky, L., Zhang, J., and Bolton, E. E., “PubChem 2019 update: Improved access to chemical data,” (2019).